

Hollow cathode effect modified time-dependent global model and high-power impulse magnetron sputtering discharge and transport in cylindrical cathode

Cite as: J. Appl. Phys. **125**, 063302 (2019); <https://doi.org/10.1063/1.5048554>

Submitted: 16 July 2018 . Accepted: 24 January 2019 . Published Online: 12 February 2019

Suihan Cui, Zhongzhen Wu, Hai Lin, Shu Xiao, Bocong Zheng, Liangliang Liu, Xiaokai An, Ricky K. Y. Fu, Xiubo Tian, Wenchang Tan, and Paul K. Chu 



[View Online](#)



[Export Citation](#)



[CrossMark](#)

ARTICLES YOU MAY BE INTERESTED IN

Strain measurement of ultrathin epitaxial films using electron diffraction techniques
Journal of Applied Physics **125**, 082401 (2019); <https://doi.org/10.1063/1.5049357>

Dissociative recombination process of ammonium for HN-MAR in high density D-N plasmas
Physics of Plasmas **25**, 123510 (2018); <https://doi.org/10.1063/1.5056204>

Experimental and computational investigations of the effect of the electrode gap on capacitively coupled radio frequency oxygen discharges
Physics of Plasmas **26**, 013503 (2019); <https://doi.org/10.1063/1.5063543>

Ultra High Performance SDD Detectors



See all our XRF Solutions

Hollow cathode effect modified time-dependent global model and high-power impulse magnetron sputtering discharge and transport in cylindrical cathode

Cite as: J. Appl. Phys. 125, 063302 (2019); doi: 10.1063/1.5048554

Submitted: 16 July 2018 · Accepted: 24 January 2019 ·

Published Online: 12 February 2019



Suihan Cui,¹ Zhongzhen Wu,^{1,2,a)} Hai Lin,¹ Shu Xiao,¹ Bocong Zheng,¹ Liangliang Liu,¹ Xiaokai An,¹ Ricky K. Y. Fu,² Xiubo Tian,¹ Wenchang Tan,¹ and Paul K. Chu²

AFFILIATIONS

¹School of Advanced Materials, Peking University Shenzhen Graduate School, Shenzhen 518055, China

²Department of Physics and Department of Materials Science and Engineering, City University of Hong Kong, Kowloon, Hong Kong, China

^{a)}Author to whom correspondence should be addressed: wuzz@pkusz.edu.cn. Tel./Fax: +86-755-26032957.

ABSTRACT

High-power impulse magnetron sputtering boasts high ionization, large coating density, and good film adhesion but suffers from drawbacks such as low deposition rates, unstable discharge, and different ionization rates for different materials. Herein, a cylindrical cathode in which the special cathode shape introduces the hollow cathode effect to enhance the discharge is described. To study the discharge performance of the cylindrical cathode, a hollow cathode effect modified time-dependent global model is established to fit the discharge current pulses. The simulation results indicate that the cylindrical cathode has relatively large Hall parameters of 24 (700 V) to 26 (1000 V). Compared to the planar cathode, the cylindrical cathode has a larger plasma density as a result of the hollow cathode effect. In addition, the ionization rate and ion return probability increase by about 3.0% and 4.3%, respectively. Particle transport derived from the plasma diffusion model shows that the magnetic field enables further diffusion of ions than atoms, resulting in nearly pure ion deposition on the substrate. The deposition rate and ion current measured experimentally support the simulation model and results, and this model provides a universal platform to simulate plasma systems with similar structures.

Published under license by AIP Publishing. <https://doi.org/10.1063/1.5048554>

I. INTRODUCTION

High-power impulse magnetron sputtering (HiPIMS)^{1–3} has advantages such as high ionization rates of the sputtered materials,^{4–6} easy control of electromagnetism,⁷ and the deposition of high-performance coatings.^{8–12} However, intrinsic disadvantages¹³ of HiPIMS such as the low deposition rate,⁹ unstable discharge,⁷ and different ionization rates for different materials¹⁴ have hampered wider industrial applications. To improve the discharge and deposition rate, modulated pulsed power magnetron sputtering (MPPMS)¹⁵ and HiPIMS coupled with direct current (DC),¹⁶ radio frequency (RF),¹⁷ and medium frequency (MF)¹⁸ have been proposed, but there is a

compromise between the deposition rate and ionization.¹⁹ Recently, inspired by the macro-particle filtering technique in cathodic arc ion plating,²⁰ a cylindrical cathode has been developed and shows potential in circumventing the aforementioned limitations.^{21,22} However, the HiPIMS discharge and transport details pertaining to the cylindrical cathode are not well known due to the experimental difficulty in plasma diagnostics.

To investigate the discharge and transport details in the sputtering process, several simulation models such as the analytical model,^{23,24} hydrodynamic model,^{25–27} particle-in-cell/Monte Carlo collision (PIC/MCC) model,^{28,29} and global

model^{30–32} have been proposed. As a classical model, the global model first proposed by Lieberman and Gottscho³³ describes the discharge of noble gas and has been extended to molecular gas discharge by Lee *et al.*^{34,35} to estimate the discharge state and calculate the plasma constituents via particle balance and energy conservation. Gudmundsson developed a time-dependent global model³⁶ for HiPIMS discharge simulation based on the Ar and metal particle discharge model,³⁷ and the region in front of the target was employed by Samuelsson *et al.*⁹ to study the ionization rate of different target materials. However, with regard to HiPIMS discharge in the cylindrical cathode, these models cannot accurately describe the particle balance equations because of the large influence of the hollow cathode effect on the macroscopic parameters of the HiPIMS discharge.

In this work, the discharge enhancement arising from the hollow cathode effect in the cylindrical cathode is qualitatively verified and quantitatively calculated by the PIC/MCC method. A hollow cathode effect modified time-dependent global model is proposed together with the plasma diffusion model, and the discharge and transport during a reactive HiPIMS pulse are systematically studied. The deposition rates and ion currents of the cylindrical cathode measured from discharges at 600–1000 V and 1.0 Pa experimentally agree with the simulation results and confirm the validity of the model.

II. DISCHARGE EXPERIMENTS

The discharge experiment was performed in the home-made vacuum system^{20,21} with dimensions of 600 mm × 600 mm × 500 mm equipped with a power source developed by the Harbin Institute of Technology (HIT) for HiPIMS. The output voltage was 0–1000 V, the pulse frequency was 50–300 Hz, and the pulse width was 50–400 μ s. The cylindrical source inner diameter was 120 mm, the outer diameter was 190 mm, and the height was 60 mm. The target [see Fig. 4(f)] in the source was cylindrical and made of copper (99.9%). The inner diameter was 120 mm, the outer diameter was 132 mm, and

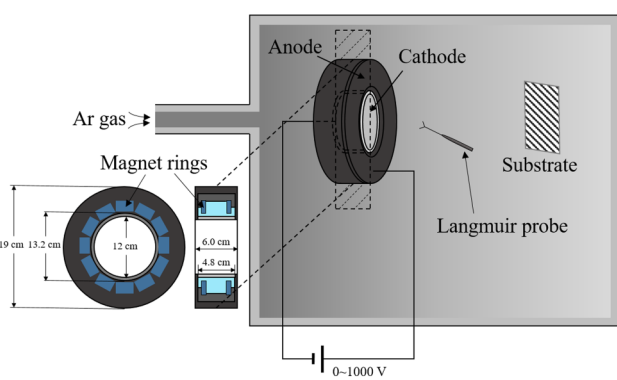


FIG. 1. Schematic of the vacuum devices.

the height was 48 mm. Magnetic fields were created by a magnet ring consisting of several small rectangular magnets. The gas was high-purity argon (99.99%), and the pressure was 1×10^{-3} Pa. During the discharge experiment, the HiPIMS power supply provided a power of 2 kW to the target with 300 μ s pulses at a frequency of 50 Hz. Figure 1 shows the schematic of the apparatus. The deposition time for each sample was 20 min, and the thickness was measured by a profilometer. The coatings were deposited at 1 Pa using an argon flow rate of 8 SCCM. The ion current was measured at a distance of 15 cm from the outlet of the cylindrical cathode by a Langmuir probe.

III. SIMULATION METHODS

A. PIC/MCC method

The PIC/MCC method is used to preliminarily simulate the initial gas (Ar) discharge process of the planar cathode and cylindrical cathode. The procedures which include editing and calculation are operated by MATLAB. The initial plasma density is uniform with the value of 10^{13} l/m^3 , the voltage is 800 V, the pressure is 1 Pa, and the temperature is 300 K. The initial energy distributions of each particle follow the Maxwell-Boltzmann distribution, and the initial condition is equivalent to that when no discharge occurs. To reduce the calculation burden, several assumptions are proposed to simplify the model. Firstly, the planar cathode is considered as a two-dimensional model, while the simulated region of the cylindrical cathode is a rotated section in cylindrical coordinates because of the symmetry. The direction perpendicular to the simulated region is also considered when the particle velocity is calculated. Secondly, the magnetic field of the two kinds of cathodes is consistent. Thirdly, the simulated particles are only electrons and Ar ions, whereas the density of the background gas (Ar) is constant. The reactions and rate coefficients are shown in Table II. The mesh cells are programmed to be smaller and smaller during the discharge process. At the beginning of the discharge, the mesh cell size is $1 \times 1 \text{ mm}^2$ since the Debye length is large. As the plasma density is increased, the Debye length decreases gradually. The program checks the Debye length in every 10 ion time step calculation and reduces the mesh cell when the Debye length is smaller than the mesh cell size. Therefore, the mesh cell size in the ionization region ($4 \text{ cm} \leq r \leq 6 \text{ cm}, 2 \text{ cm} \leq z \leq 4 \text{ cm}$) is reduced to $10 \times 10 \mu\text{m}^2$ at last. The time step of electrons is $1 \times 10^{-7} \text{ s}$, and the time step of ions is $1 \times 10^{-11} \text{ s}$. The self-consistent potential is calculated by Poisson's equation for every ion time step. The magnetic field is provided by the magnets. It is invariable and unrelated to the particle movement.

B. Hollow cathode effect modified time-dependent global model

To establish the global plasma model, the main participant particles and key reactions during the discharge process need to be identified. In the Ar/Cu discharge system, the

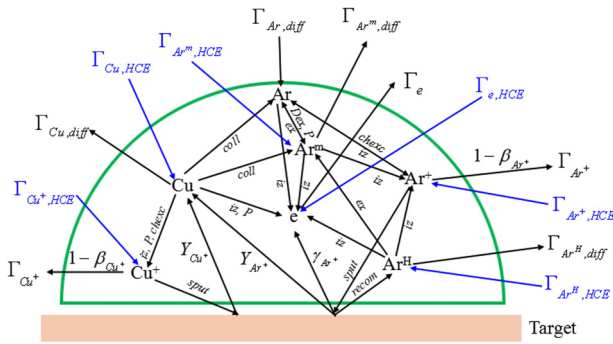


FIG. 2. Schematic diagram of the hollow cathode effect modified global model showing the particle balance and corresponding reactions in the ionization region. The subscripts are defined as follows: diff (diffusion), ex (excitation), Dex (deexcitation), iz (ionization), P (Penning ionization), chex (charge exchange), coll (collision), recom (recombination), sput (sputtering), and HCE (hollow cathode effect).

main particles include cold electrons (e), hot electrons (e^H), ground state atoms (Ar and Cu), energetic atoms (Ar^H), metastable atoms (Ar^m), and ionized state ions (Ar^+ and Cu^+). The schematic of the particle equilibrium reactions are shown in Fig. 2, and more details can be found in the literature.³⁸ The reactions and rate coefficients are given in Table III. The difference is that some participating particles except Ar atoms return to the ionization region because of the hollow cathode effect, as displayed in Eqs. (A2)–(A7). The blue terms $\Gamma_{M,HCE}$ stand for the flux coming to the ionization region from the opposite part of the target. The Hall parameter, $\omega\tau$, denoting the ratio of the electron cyclotron frequency to collision frequency, is the fitting parameter in the modified global model. Based on the glow area and corrosion ring in the experiment, the radius of the ionization region R_{IR} is measured and set to be 1.5 cm. In the cylindrical cathode, the contact area of the ionization region with the target S_T (m^2), ionization region superficial area S_{IR} (m^2), and ionization region volume V_{IR} (m^3) can be calculated by integration as shown in Eq. (1), where R_{source} (equal to 6 cm) is the radius of the cylindrical cathode

$$S_T = 4\pi R_{source} R_{IR},$$

$$S_{IR} = \int_0^{\frac{\pi}{2}} 4\pi R_{IR} [R_{source} - R_{IR} \cos(\theta)] d\theta + S_T, \quad (1)$$

$$V_{IR} = \int_0^{\frac{\pi}{2}} 4\pi [R_{source} - R_{IR} \cos(\theta)] R_{IR}^2 \sin^2(\theta) d\theta.$$

C. Plasma diffusion model

To study the transport properties of the particles produced by the cylindrical cathode, a plasma diffusion model is developed as shown in Fig. 3. The plasma is assumed to be ionized in the red semicircle (same as the ionization region of the global model), which is defined as the ionization region.

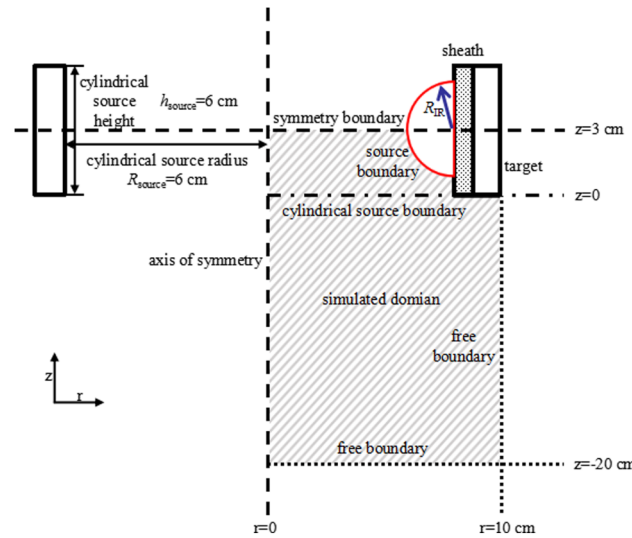


FIG. 3. Schematic diagram of the plasma diffusion model.

In the simulated domain, diffusion is treated as the main way of plasma transport and the electron temperature T_e (V) in the simulated domain is a constant calculated by the aforementioned global model. During diffusion, elastic collisions between metal particles (Cu and Cu^+) and background Ar are taken into consideration. Ionization in front of the substrate is not considered since the Cu^+ density is much less than the Cu^+ density in front of the substrate, and there are few effects due to the ionization events on the ion current and ionization rate. For the same reason, the ion-neutral charge exchange or elastic collisions ($Cu^+ + Cu \Rightarrow Cu + Cu^+$, $Cu^+ + Cu \Rightarrow Cu^+ + Cu$) are not considered in this work. Therefore, the plasma diffusion can be described by the equation of continuity as shown in Eq. (2), where n ($1/m^3$) is the plasma density and Γ [$1/(m^2 s)$] is the flux of the plasma density:

$$\frac{\partial n}{\partial t} + \text{div}(\Gamma) = 0, \quad (2)$$

$$\Gamma = -D\nabla n.$$

For Cu^+ , the ion diffusion coefficient has two components, one parallel to the magnetic field $D_{||}$ and the other perpendicular to the magnetic field D_{\perp} . According to the force states of the charge, they are expressed as $D_{||} = \frac{eT_e}{m_{Cu}v_{Cu^+}}$ and $D_{\perp} = \frac{D_{||}}{1+(\omega\tau)^2} = \frac{\pi}{8}\bar{r}_c^{-2}v_{Cu^+}$,³⁹ respectively, in which v_{Cu^+} is the collision frequency of Ar and Cu^+ , $\omega\tau$ is the Hall parameter which can be fitted by the modified global model, and \bar{r}_c is the mean gyroradius which is inversely proportional to the magnetic induction intensity.

There are three boundary conditions in the simulated domain. According to Fig. 2, the symmetrical boundary

condition contains the axis of symmetry ($r = 0$) and the symmetry boundary ($z = 3 \text{ cm}$), which can be described by Eqs. (3) and (4), respectively.

$$\frac{\partial n}{\partial r} = 0, \quad r = 0 \quad (3)$$

and

$$\frac{\partial n}{\partial z} = 0, \quad z = 3 \text{ cm}. \quad (4)$$

The source boundary is the interface between the ionization region and simulated domain. The Cu^+ density of the ionization region and the simulated domain is the same, as shown in Eq. (5):

$$n = n_{\text{Cu}^+, 0}. \quad (5)$$

The other boundaries are the free boundaries from which ions leave the simulated region with the Bohm velocity.⁹ They

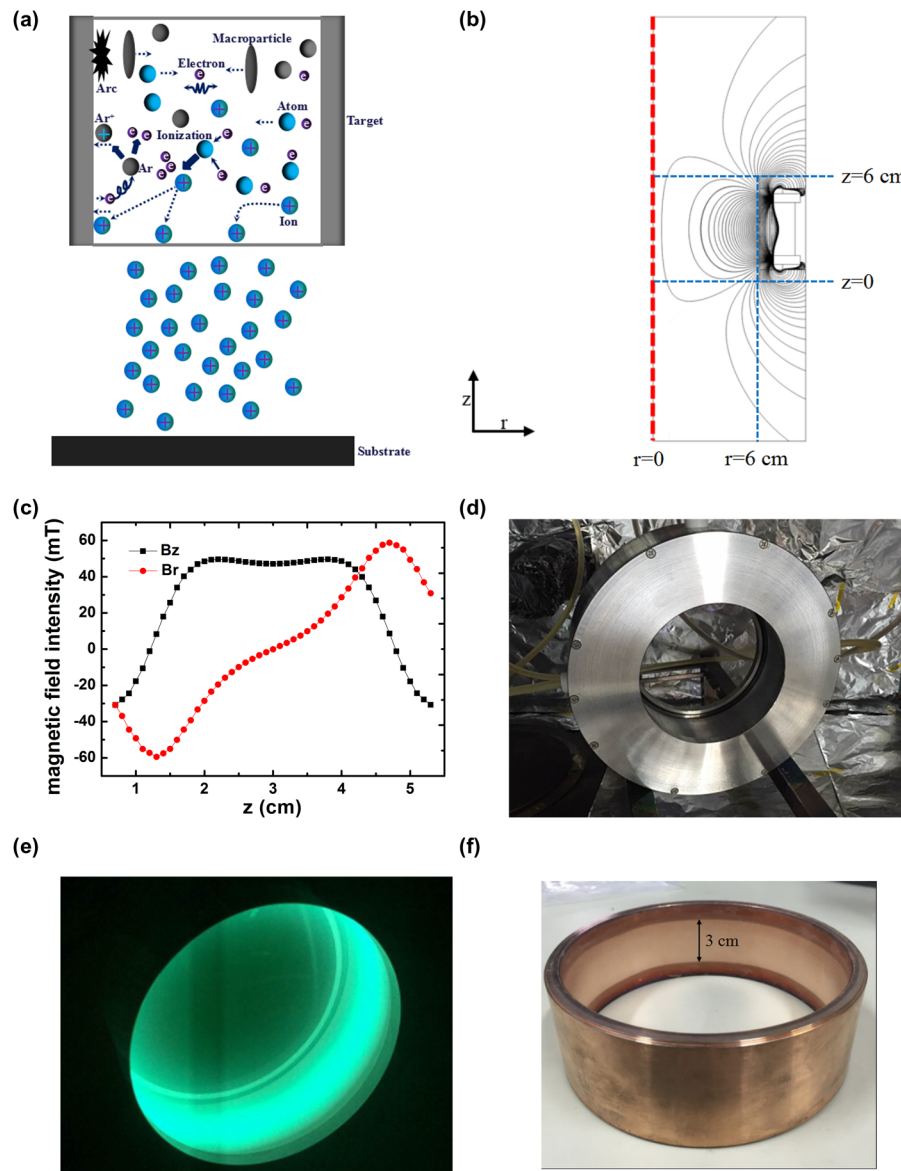


FIG. 4. (a) Schematic diagram, (b) simulated magnetic induction line distribution, (c) magnetic field on the target, (d) physical picture, (e) glow picture, and (f) target etching of the cylindrical cathode. The red dashed line represents the central symmetry axis.

are described as follows:

$$\Gamma = -nv_{bohm}, \quad (6)$$

where $v_{bohm} = \sqrt{\frac{eT_e}{m_{Cu}}}$.

Diffusion of the Cu neutrals follows the equation of continuity [Eq. (2)]. The diffusion coefficient is estimated by $D_{Cu} = \frac{k_B T}{m_{Cu} v_{Cu}}$, where k_B is Boltzmann's constant, T is the temperature, m_{Cu} is the Cu atom mass, and v_{Cu} is the collision frequency between Cu atoms and argon atoms. At the source boundary, the Cu density of the ionization region and diffusion region is the same as shown in Eq. (7):

$$n = n_{Cu,0}, \quad (7)$$

where $n_{Cu,0}$ can be calculated from the global model. The atoms are assumed to leave the simulated region with the thermal velocity and the free boundaries are described by Eq. (8):

$$\Gamma = -nv_{thermal}, \quad (8)$$

where the thermal velocity is estimated by $v_{thermal} = \sqrt{\frac{3k_B T}{m_{Cu}}}$.

IV. RESULTS AND DISCUSSION

Figure 4(a) shows the hollow cathode effect of the cylindrical cathode.^{20,21} The cylindrical structure limits the discharge to the inside of the cylindrical cathode avoiding deposition of large particles produced by arcing during the HiPIMS discharge on the substrate that can destroy the coating. Electrons continue to move back and forth in the cylindrical cathode leading to a higher collision frequency and larger plasma density. Some of the metallic ions leave the ionization region and out of the cylindrical cathode by the magnetic system, and some other metallic ions move to the opposite target producing repeated sputtering. The unionized atoms continue to move in the cylindrical cathode because of two-side sputtering until ionization before escaping the cylindrical cathode. To avoid arcing induced by sputtered materials deposited on the cathode with conventional three row magnets, two row magnets are used in our new cathode, as shown in Fig. 4(b). The magnetic field of the cylindrical cathode is simulated, and the critical shape size of the cylindrical cathode is optimized. To obtain effective sputtering, the inner diameter and height of the cylindrical cathode are 120 mm and 60 mm, respectively. The effective discharge width (tangential magnet field B_z between 30 and 50 mT) is about 3 cm and the mean tangential magnetic intensity is 45 mT, as shown in Fig. 4(c). Based on the simulation, the cylindrical cathode is processed as shown in Fig. 4(d). Copper is used to evaluate the HiPIMS discharge in argon, and the glowing image is displayed in Fig. 4(e). The glow is bright green indicating a stable and strong discharge in the presence of large-density Cu. The etching shape of the target is a

uniform ring according to Fig. 4(f). The etching width is 3 cm corresponding to the simulated tangential magnet field on the target in Fig. 4(c).

To investigate the ionization region shape and hollow cathode effect, the PIC/MCC method is used to simulate the initial gas (Ar) discharge process (800 V, 1 Pa, 0–3 × 10⁻⁷ s) and calculate the distribution of the plasma density, as shown in Fig. 5 and Table I. Here, we do not consider the metallic particles (only gas) in this part of the simulation for simplicity since it cannot change the hollow cathode effect. Therefore, the electron density is generally equal to that of the Ar⁺ in the ionization region. The ionization region before the target is approximately a semicircle consistent with the fundamental assumption of the global model. The largest plasma density in the cylindrical cathode is 1 × 10¹⁸ 1/m³ which is nearly an order of magnitude larger than that of the planar cathode for the same discharge time (3 × 10⁻⁷ s). Besides, the ionization region of the cylindrical cathode is larger than that of the planar cathode resulting in a larger etching area. Since the simulation conditions such as the discharge voltage (800 V), pressure (1 Pa), and magnetic field on the target [Figs. 4(b) and 4(c)] are the same, the hollow cathode effect introduced by the cathode shape turns out to be the main reason for the discharge enhancement. It can be explained by the left boundary condition of the solution domain in Figs. 5(a) and 5(c). The left boundary of the cylindrical cathode is the symmetry axis and the electrons bounce back. Meanwhile, in the planar cathode, the left boundary is a free one across which electrons disappear from the solution domain, and consequently, a larger plasma density and stronger discharge are formed in the cylindrical cathode in the beginning of the discharge.

To further analyze the HiPIMS discharge process of the cylindrical cathode, the global model is used to fit the experimental current waveforms [Fig. 6(b)]. The discharge voltage is varied from 600 to 1000 V, and the pressure is 1 Pa. The discharge currents are stable and strong and increase with the discharge voltage. Compared to the pulse voltage, a delay of about 40 μs is observed from the discharge current, and afterwards, the discharge threshold is broken and the currents go up speedily with discharge time.⁴⁰

According to the PIC/MCC results, the hollow cathode effect is considered in the global model and the hollow cathode effect modified time-dependent global model (Fig. 2) is established. To ensure the accuracy, it is necessary to investigate the proportion c of the reaction particles influenced by the hollow cathode effect. Here, the parameter “ c ” is the ratio of the particles that flow out of the ionization region and go into the ionization region of the opposite part of the target to all the particles leaving the ionization region. It can be obtained by analyzing thousands of particle tracks based on the PIC/MCC results. The calculation results are about 0.125 for ions and 0.250 for electrons. The neutral atoms are calculated independently with the results of the particles' distributions in the PIC/MCC modes as the background. The atoms are released from the target, and their tracks are analyzed considering collisions with particles in the background. c is the ratio of the atoms which come from the target and

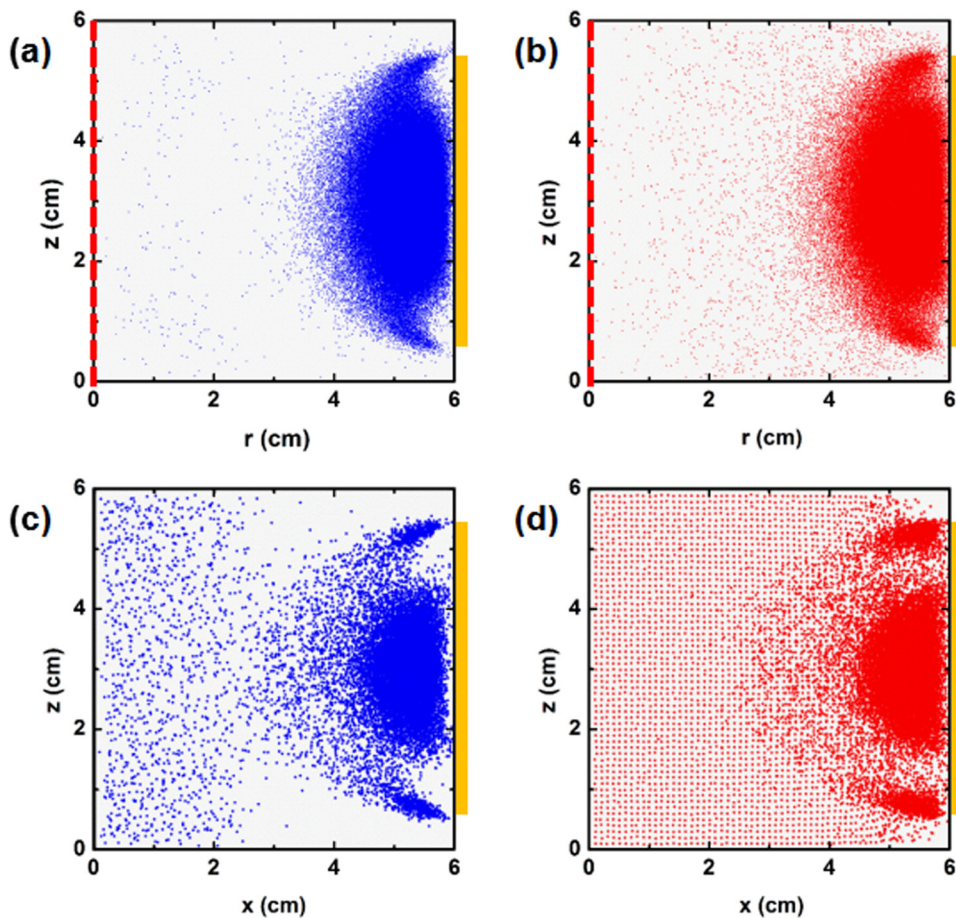


FIG. 5. Distributions: (a) Electrons and (b) Ar ions in the cylindrical cathode; (c) electrons and (d) Ar ions the planar cathode at 3×10^{-7} s. The red dashed line is the symmetry axis and the ionization region is approximately a semicircle. The orange domain stands for the target.

go into the opposite ion regions and is 0.210. Therefore, the hollow cathode effect enhancement (blue terms in Fig. 2) can be described by Eq. (9):

$$\begin{aligned} \Gamma_{M,HCE} &= c\Gamma_{M,diff}, \quad M = Cu, Ar^m, Ar^H, \\ \Gamma_{Mi,HCE} &= c\Gamma_{Mi}, \quad Mi = Cu^+, Ar^+, e. \end{aligned} \quad (9)$$

To evaluate the hollow cathode effects on the HiPIMS discharge, the discharge at 900 V and 1 Pa is simulated by

TABLE I. Numerical results of the ionization region derived from the PIC/MCC model.

	Average plasma density ($1/m^3$)	Ionization region radius (cm)
Cylindrical cathode	1.2×10^{18}	1.5
Planar cathode	4.5×10^{17}	1.2

both the modified global model and ordinary global model³⁸ as shown in Fig. 7. A high Ar density can be observed at the beginning of the pulse, but it declines quickly in the next 50 μ s. On the other hand, Ar^+ increases after the pulse shows a peak at about 40 μ s and decreases again. The small Ar density may stem from the strong rarefaction effect because of the high intensity discharge when Ar is introduced from the vacuum inlet away from the cylindrical cathode. Cu produced by sputtering from the target shows a significant increase following Ar and becomes saturated at about 120 μ s. There is an obvious delay in the process indicating intense ionizing of Cu^+ at 40–60 μ s, and they become the main particles in the plasma. The densities of Cu and Cu^+ calculated by the modified global model are larger than those by the ordinary global model demonstrating enhanced sputtering and ionization as a result of the hollow cathode effect of the cylindrical cathode. The densities of Ar and Ar^+ show very small differences because of the small amount of gas in the intense discharge zone. The ionization rate α and ion return probability β are

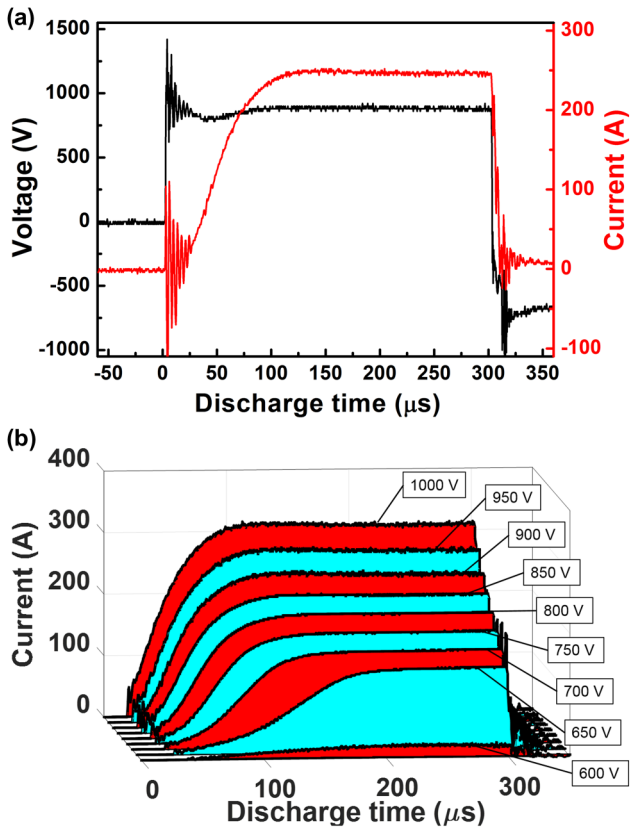


FIG. 6. (a) Current and voltage in a pulse at 900 V and 1 Pa. (b) Current pulse shape at different pulse voltages in the Cu HiPIMS discharge in argon at 1 Pa.

simulated and shown in Fig. 7(b). Because of repeated sputtering and ionization of unionized particles inside the cylindrical target, the ionization rate α calculated by the modified model reaches 74.0%, about 3.0% larger than that without the hollow cathode effect. The ion return probability β calculated by the modified model reaches 65.8%, an increase of about 4.3%. Therefore, the global model must be modified by incorporating the hollow cathode effect to simulate the discharge in the cylindrical cathode.

The HiPIMS discharge properties of the cylindrical cathode are simulated by the hollow cathode effect modified global model. The Hall parameter $\omega\tau$, a fitting parameter in the global model, represents the ratio of Hall current to the discharge current, which can be calculated as shown in Fig. 8(a). By selecting $\omega\tau$ to be from 10 to 30, fitting of the discharge current shows $\omega\tau=25.5$, which means that the modeled discharge process in a pulse is consistent with the real physical situation. Figure 8(b) reveals that $\omega\tau$ goes up from 24 (700 V) to 26 (1000 V), indicating enhanced cyclotron electron motions by the discharge voltage. It has been reported that the Hall parameter $\omega\tau$ of the “Bohm-like” diffusion plasma lies

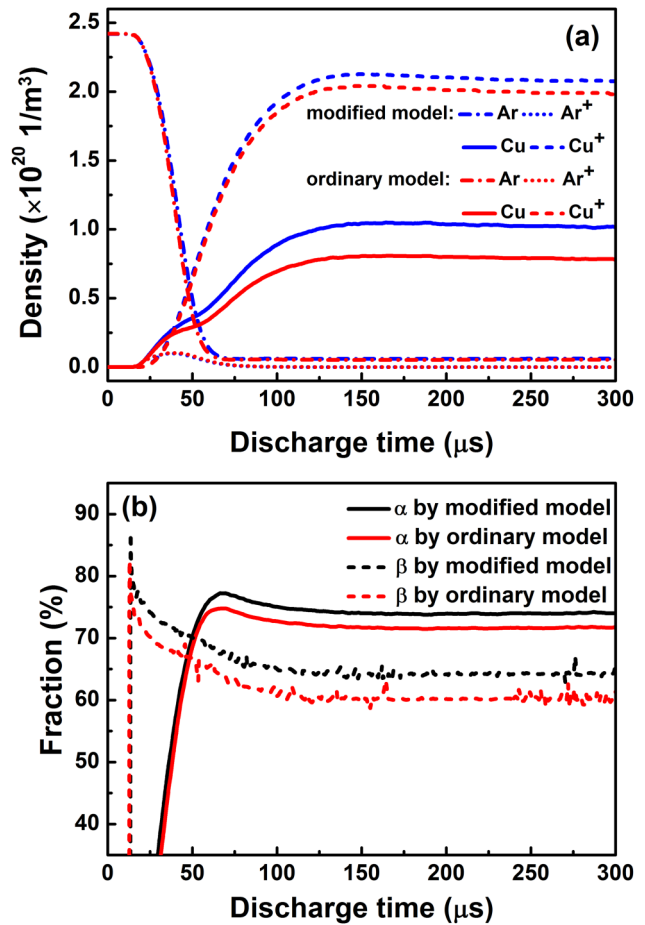


FIG. 7. (a) Main particles density and (b) ionization rate α of sputtered Cu atoms and ion return probability β simulated by the ordinary global model and the modified global model.

between 8 and 30.^{41,42} The Hall parameter of the cylindrical cathode falls in the range and is relatively large. For comparison, the HiPIMS discharge current pulse waveforms of the planar cathode at 900 V and 1 Pa are simulated, and the results show that the Hall parameter of the planar cathode is about 18 which is smaller than that of the cylindrical cathode. The reason may be that a large amount of particles influenced by the hollow cathode effect participate in the discharge process and become a part of the Hall current in the cylindrical cathode. All in all, the hollow cathode effect enhances the discharge by increasing the Hall current.

The HiPIMS discharge dependence on the discharge voltage is shown in Fig. 9. Like the discharge current, the particle density of Cu⁺ and Cu shows a delay (delay 1) compared to the discharge voltage and the delay becomes smaller with increasing discharge voltage. Delay 2 occurs because a large amount of Cu atoms are ionized to form Cu ions quickly

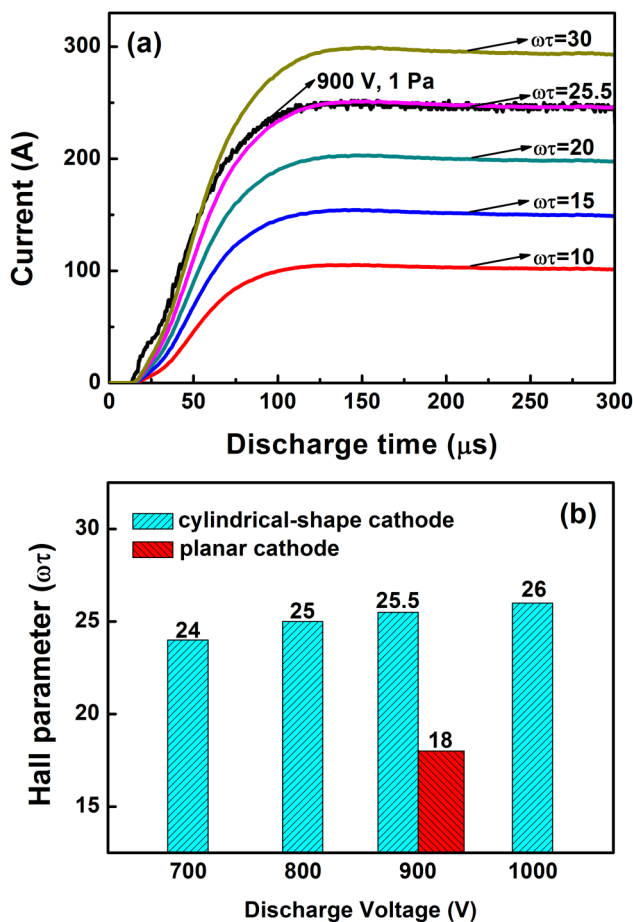


FIG. 8. (a) The experimental and fitted discharge currents at 900 V and 1 Pa, and the fitting parameters $\omega\tau$ is from 10 to 30. (b) Hall parameter $\omega\tau$ fitted by the global model at different discharge voltages.

consuming Cu atoms which cannot be replenished by simultaneous sputtering. With increasing discharge voltage, sputtering is enhanced further, resulting in faster replenishment and narrower delay 2. The largest densities of Cu^+ and Cu are $2.8 \times 10^{20} \text{ 1/m}^3$ and $1.4 \times 10^{20} \text{ 1/m}^3$, respectively, and larger than those of the planar cathode in HiPIMS discharge previously reported ($\sim 10^{19} \text{ 1/m}^3$).³⁸ The densities of Cu^+ and Cu increase with the voltage as consistent with the Hall parameter $\omega\tau$ since the Hall current enhances the discharge. The electron temperature T_e exhibits an opposite tendency compared to the Cu^+ density with voltage as shown in Fig. 9(c). The discharge intensity and sputtering are enhanced by a larger discharge voltage, resulting in much more electron collisions which can reduce the electron temperature.^{38,43} Therefore, the planar cathode has the largest electron temperature in the steady state.

According to the simulation results of the modified global model at 1000 V and 1 Pa, plasma transport in front of the

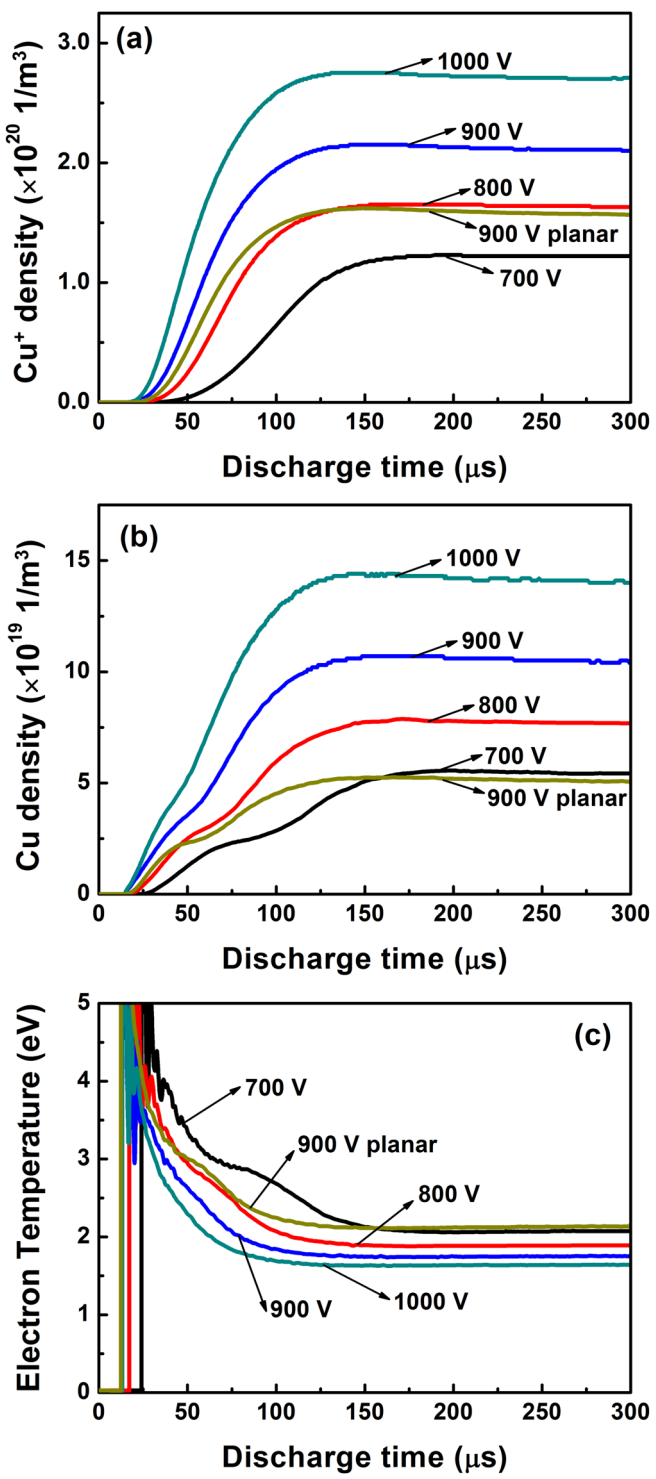


FIG. 9. Simulation results: (a) Cu^+ density, (b) Cu atoms density, and (c) electron temperature for different discharge voltages obtained by the modified global model.

cylindrical cathode is simulated by the plasma diffusion model. The distributions of Cu^+ and Cu are shown in Figs. 10(a) and 10(b), respectively. Because the magnetic field restrains electron movements and the electrostatic interactions between ions and electrons keep the electric neutrality in the plasma, Cu^+ shows almost the same distributions as electrons. According to the ion diffusion coefficient equation, $D_{\perp} \ll D_{||}$

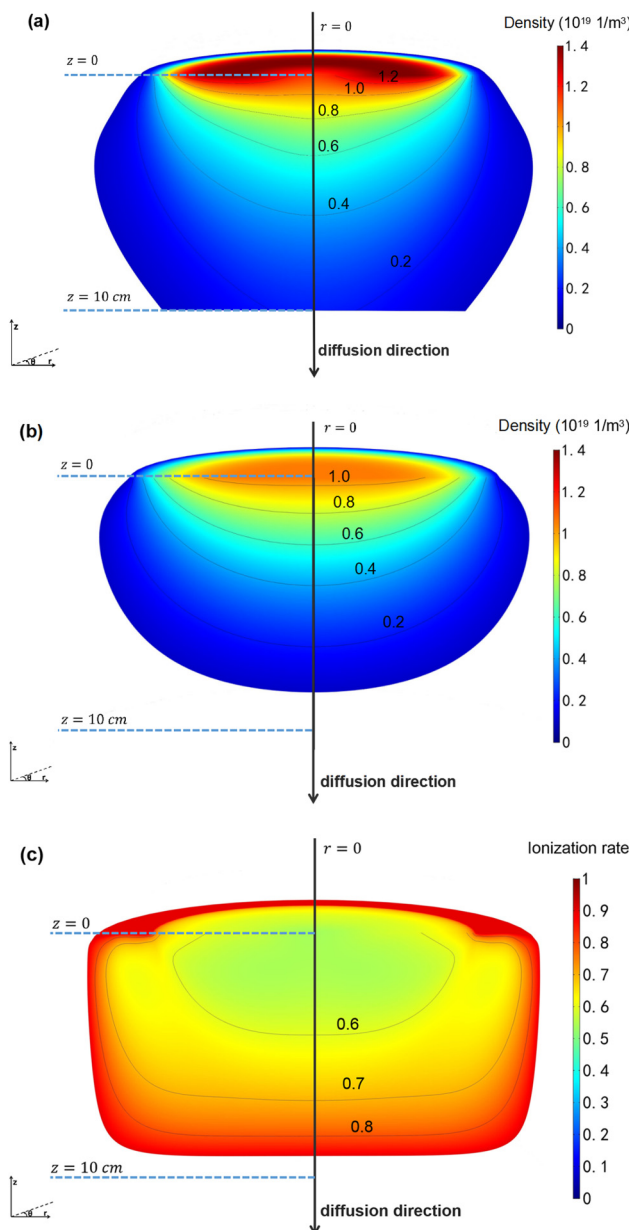


FIG. 10. Transport in front of the cylindrical cathode at 1000 V and 1 Pa: (a) Cu^+ , (b) Cu, and (c) ionization rate. The gray arrow line shows the diffusion direction along the symmetry axis.

because $\omega\tau \gg 1$. Therefore, ions tend to diffuse along the magnetic induction lines. According to the magnetic field distribution shown in Fig. 4(b), Cu^+ diffuses mainly along the z direction along the symmetry axis. On the edge of the cylindrical cathode, Cu^+ diffuses mainly along the r direction. Therefore, Cu^+ initially moves to the symmetry axis and then along the symmetry axis. This is why an angle on the symmetry axis is observed from the contour lines of the Cu^+ density. Different from Cu^+ , diffusion of Cu is not influenced by the magnetic field. Since the Cu diffusion coefficient is isotropic, the contour lines of the Cu density are smooth. The ionization rate denoting the Cu^+ proportion is shown in Fig. 10(c). Cu^+ can diffuse to a larger distance due to the magnetic field than Cu, resulting in increased ionization along the symmetry axis. Consequently, a nearly pure ion deposition process can be achieved on the substrate by selecting the deposition location. The ionization rate is also large at the boundary of the solution domain as the Cu density is too small.

To assess the accuracy of the plasma transport simulation, the ion currents and deposition rate are measured. The density $n_{\text{Cu}^+,0}$ at the source boundary determines the ion current because the Cu^+ density at the source boundary $n_{\text{Cu}^+,0}$ is time-dependent. Therefore, the ion current is a function of the discharge time. The ion flux Γ_{ion} is calculated at the location where the Langmuir probe is placed, and the ion current I_{ion} can be obtained by Eq. (10),

$$I_{\text{ion}} = \Gamma_{\text{ion}} S_L e, \quad (10)$$

where S_L is the test area of the Langmuir probe. The red line in Fig. 11(a) presents the simulation results of the ion currents derived from the ion density evolution for a pulse at a distance of 15 cm from the cylindrical cathode. A delay of about 100 μs is observed from the ion current and 50 μs later than that of the discharge current, indicating that the ion diffusion time is about 50 μs . The ion current increases monotonically with the discharge until the discharge is over, and there is an inflection point in the ion current at about 300 μs because the increase in the ion current is slowed. However, the ion current increases and reaches the maximum value at 370 μs because of the delay between the largest plasma density in the cylindrical cathode and near the probe and it drops rapidly afterwards. The ion currents measured by a Langmuir probe are in good agreement with the simulation as shown in Fig. 11(a). The deposition rates at different distances from the cathode can be calculated by integrating the plasma density gradient on the symmetry axis with the discharge time, as shown by the red line in Fig. 11(b). The deposition rate decreases with increasing distance between the substrate and cylindrical cathode. The maximum and minimum deposition rates are 700 nm/min and 30 nm/min, respectively. A Si (100) substrate with a diameter of 1.5 cm is put along the central symmetry axis at different distances from the cathode, and the deposition rates in the same discharge conditions are measured as shown in Fig. 11(b). Generally, the experimental deposition rates are consistent with the simulation results. However, the simulation result is a little larger when the distance is less than

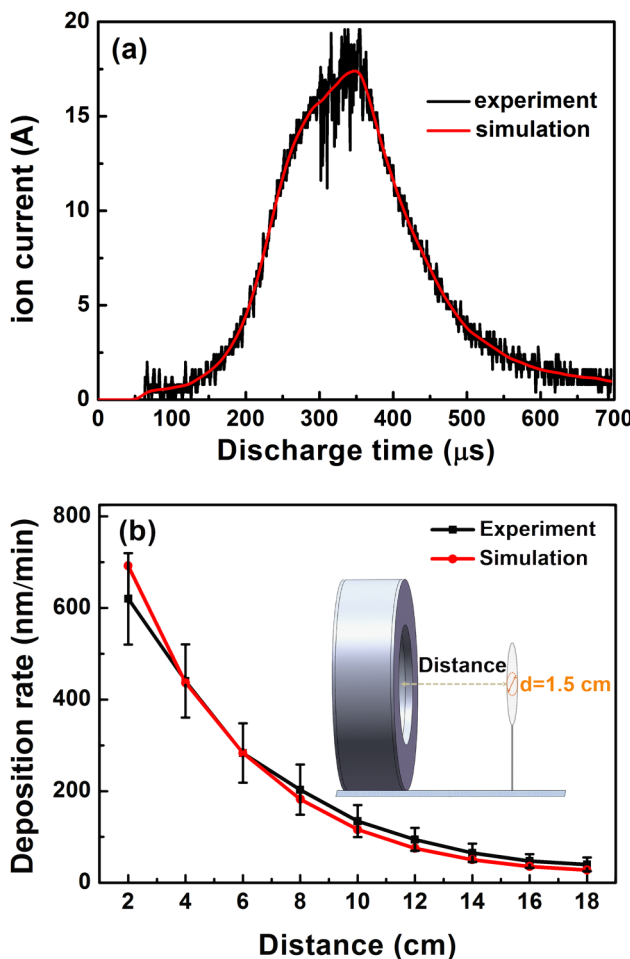


FIG. 11. (a) Ion currents obtained by experiments and simulation at 1000 V and 1 Pa. (b) Deposition rates measured by experiments and simulation versus the distance between the substrate and cylindrical cathode at 1000 V and 1 Pa.

4 cm, but the experimental result is slightly bigger when the distance is larger than 7 cm. The errors in the deposition rates may be because the simulation ignores the influence of the substrate on the plasma distribution.

V. CONCLUSION

To investigate the HiPIMS discharge and transportation in the cylindrical cathode, systematic simulation and experiments are performed. The hollow cathode effect introduced by the cylindrical cathode enhances the discharge. Simulation of the particle tracks show that about 10%–25% of the particles return to the ionization region during the discharge process. The hollow cathode effect modified global model is established and reveals that the cylindrical cathode produces a high plasma density of $1 \times 10^{20} \text{ l/m}^3$ and Hall parameters of 24 (700 V) to 26 (1000 V), which are larger than those of the planar cathode. In

addition, the ionization rate and ion return probability increase by about 3.0% and 4.3%, respectively. The plasma diffusion model is developed, and the results suggest that nearly pure ion deposition occurs on the substrate. The ion currents and deposition rates experimentally determined match the simulation results. The hollow cathode effect modified global model and diffusion model described here can be extended to other structures, and the cylindrical cathode has large potential in industrial applications of HiPIMS.

ACKNOWLEDGMENTS

This work was financially supported by the Guangdong Science and Technology Research Grants (No. 2015B090927003), the Shenzhen Science and Technology Research Grants (Nos. JCYJ20150828093127698 and JCYJ20170306165240649), the Hong Kong Research Grants Council (RGC) General Research Funds (GRG) (No. CityU 11205617), and the City University of Hong Kong Strategic Research Grant (SRG) (No. 7005105).

APPENDIX: RATE COEFFICIENTS AND PARTICLE BALANCE EQUATION

The reactions and rate coefficients of the PIC/MCC model are shown in Table II. The reactions in Ar/Cu discharge plasma and the corresponding reaction rate coefficients in the equations are shown in Table III.

The particle densities can be described by considering the generation and the loss of each particle as shown in Fig. 1. Based on the model described in our previous work,³⁸ the equation of Ar^+ , Ar^m , Ar^H , Cu , Cu^+ , the electron is modified by the hollow cathode effect in the calculation. The significance of each parameter is described in Ref. 38. In the following equations, n is the density, m is the mass, and Γ is the flux of the corresponding species. k is the reaction coefficient that can be calculated from Table III.

1. Particle balance for Ar and Cu species

For the working gas Ar, the rate equation is

$$\begin{aligned} \frac{dn_{\text{Ar}}}{dt} = & -(k_{iz} n_e + k_{iz^H} n_{e^H}) n_{\text{Ar}} - (k_{ex} n_e + k_{ex^H} n_{e^H}) n_{\text{Ar}} \\ & - \Gamma_{\text{Cu},\text{coll}} \frac{m_{\text{Cu}}}{m_{\text{Ar}}} \frac{n_{\text{Ar}}}{n_{\text{Ar}} + n_{\text{Ar}^m}} \frac{S_{\text{IR}} - S_{\text{T}}}{V_{\text{IR}}} + k_{\text{chexc}} n_{\text{Ar}^+} n_{\text{Cu}} \\ & + k_p n_{\text{Ar}^m} n_{\text{Cu}} + (k_{dex} n_e + k_{dex^H} n_{e^H}) n_{\text{Ar}^m} + \Gamma_{\text{Ar},\text{diff}} \frac{S_{\text{IR}} - S_{\text{T}}}{V_{\text{IR}}}, \end{aligned} \quad (\text{A1})$$

where the diffusional Ar flux $\Gamma_{\text{Ar},\text{diff}} = \frac{n_{\text{Ar},0} - n_{\text{Ar}}}{4} u_{\text{Ar}}$. $n_{\text{Ar},0}$ is the Ar density out of the ionization region and can be calculated by the Clapeyron equation. $u_{\text{Ar}} = \sqrt{\frac{8k_{\text{B}}T}{\pi m_{\text{Ar}}}}$ is the average velocity of Ar at $T = 300 \text{ K}$. $\Gamma_{\text{Cu},\text{coll}}$ stands for the collision part of the Cu and Cu^+ sputtering wind and is calculated by $\Gamma_{\text{Cu},\text{coll}} = (\Gamma_{\text{Cu},\text{sput}} + \Gamma_{\text{Cu}^+,\text{sput}}) F_{\text{coll}}$, in which $\Gamma_{\text{Cu},\text{sput}} = \frac{n_{\text{Cu}} u_{\text{r}_{\text{Cu}}}}{4}$ and $\Gamma_{\text{Cu}^+,\text{sput}} = \frac{n_{\text{Cu}^+} u_{\text{r}_{\text{Cu}^+}}}{4}$ are the sputtering wind of Cu and Cu^+ , respectively. $F_{\text{coll}} = 1 - \exp[-R_{\text{IR}} \sigma_{\text{Ar-Cu}} (n_{\text{Ar}} + n_{\text{Ar}^m} + n_{\text{Ar}^H})]$ is

TABLE II. Details of PIC/MCC model.

Assumptions	The planar cathode is considered as a two-dimensional model							
	The cylindrical cathode is a rotated section in cylindrical coordinates							
	The magnetic field of the two kinds cathode is consistent							
	The simulated particles are only electrons and Ar ions							
	The density of the background gas (Ar) is constant							
Initial value								
Initial value	Density (1/m ³)	Voltage (V)	Pressure (Pa)	Temperature (K)				
	1 × 10 ¹³	800	1	300				
Boundary condition	The magnetic field is invariable and unrelated with the particle movements							
	Electrons disappear on the target							
	Target	Ar ⁺ sputtering produces secondary electrons on the target						
		Ar atoms rebound on the target						
	Rotation axis	Particles rebound on the rotation axis						
		Particles disappear across the boundaries						
Simulation parameters								
Plasma density distribution, ionization region shape, and the parameter "c"								
Reactions	Reaction	Rate coefficient (m ³ /s)	Threshold (eV)	Reference				
	e + Ar → Ar ⁺ + 2e	$k_{iz} = 2.3 \times 10^{-14} T_e^{0.59} \exp(-17.44/T_e)$	15.76	44				
	e + Ar → Ar ^m + e	$k_{ex} = 2.5 \times 10^{-15} T_e^{0.74} \exp(-11.56/T_e)$	11.56	44				
	e + Ar → Ar + e	$k_{el} = 2.336 \times 10^{-14} T_e^{1.609} \times \exp[0.0618(\ln T_e)^2 - 0.1171(\ln T_e)^3]$	-	45				
	e + Ar ^m → Ar + e	$k_{dex} = 4.3 \times 10^{-16} T_e^{0.74}$	-11.56	44				
	e + Ar ^m → Ar ⁺ + e	$k_{miz} = 6.8 \times 10^{-15} T_e^{0.67} \exp(-4.2/T_e)$	4.2	44				

the collision probability with Ar in the ionization region. $\sigma_{\text{Ar-Cu}} = \pi(a_{\text{Ar}} + a_{\text{Cu}})^2$ is the estimated cross section of Ar-Cu collision based on the hard sphere model, and $a_{\text{Ar}} = 1.88 \text{ \AA}$ and $a_{\text{Cu}} = 1.4 \text{ \AA}$ are the atomic radii of Ar and Cu, respectively.

For Ar⁺, the rate equation is described as

$$\frac{dn_{\text{Ar}^+}}{dt} = -k_{\text{chexc}} n_{\text{Ar}^+} n_{\text{Cu}} - \Gamma_{\text{Ar}^+} \frac{S_{\text{IR}} - S_{\text{T}}}{V_{\text{IR}}} + \Gamma_{\text{Ar}^+, \text{HCE}} \frac{(S_{\text{IR}} - S_{\text{T}})}{V_{\text{IR}}} + (k_{iz} n_e + k_{iz}^H n_{e^H}) (n_{\text{Ar}} + n_{\text{Ar}^H}) + (k_{miz} n_e + k_{miz}^H n_{e^H}) n_{\text{Ar}^m}, \quad (\text{A2})$$

in which $\Gamma_{\text{Ar}^+} = 0.4 n_{\text{Ar}^+} u_{\text{bohm,Ar}^+}$ is the flux of Ar⁺ leaving the ionization region. $u_{\text{bohm,Ar}^+} = \sqrt{\frac{eT_e}{m_{\text{Ar}}}}$ is the Bohm velocity of Ar⁺.

For metastable atom Ar^m, the rate equation can be written as

$$\begin{aligned} \frac{dn_{\text{Ar}^m}}{dt} = & -(k_{miz} n_e + k_{miz}^H n_{e^H}) n_{\text{Ar}^m} - k_p n_{\text{Ar}^m} n_{\text{Cu}} \\ & - (k_{dex} n_e + k_{dex}^H n_{e^H}) n_{\text{Ar}^m} - \Gamma_{\text{Ar}^m, \text{diff}} \frac{S_{\text{IR}} - S_{\text{T}}}{V_{\text{IR}}} \\ & - \Gamma_{\text{Cu, coll}} \frac{m_{\text{Cu}}}{m_{\text{Ar}}} \frac{n_{\text{Ar}^m}}{n_{\text{Ar}} + n_{\text{Ar}^m}} \frac{S_{\text{IR}} - S_{\text{T}}}{V_{\text{IR}}} \\ & + \Gamma_{\text{Ar}^m, \text{HCE}} \frac{S_{\text{IR}} - S_{\text{T}}}{V_{\text{IR}}} + (k_{ex} n_e + k_{ex}^H n_{e^H}) (n_{\text{Ar}} + n_{\text{Ar}^H}). \quad (\text{A3}) \end{aligned}$$

TABLE III. Rate coefficients for Ar/Cu plasma.

Reaction	Rate coefficient (m ³ /s)	Threshold (eV)	Reference
e + Ar → Ar ⁺ + 2e	$k_{iz} = 2.3 \times 10^{-14} T_e^{0.59} \exp(-17.44/T_e)$	15.76	44
e ^H + Ar → Ar ⁺ + 2e	$k_{iz}^H = 8 \times 10^{-14} T_e^{0.16} \exp(-27.53/T_e)$	15.76	46, 47
e + Ar → Ar ^m + e	$k_{ex} = 2.5 \times 10^{-15} T_e^{0.74} \exp(-11.56/T_e)$	11.56	44
e ^H + Ar → Ar ^m + e	$k_{ex}^H = 3.84 \times 10^{-14} T_e^{-0.68} \exp(-22.32/T_e)$	11.56	46, 47
e + Ar → Ar + e	$k_{el} = 2.336 \times 10^{-14} T_e^{1.609} \times \exp[0.0618(\ln T_e)^2 - 0.1171(\ln T_e)^3]$	-	45
e + Ar ^m → Ar + e	$k_{dex} = 4.3 \times 10^{-16} T_e^{0.74}$	-11.56	44
e + Ar ^m → Ar ⁺ + e	$k_{miz} = 6.8 \times 10^{-15} T_e^{0.67} \exp(-4.2/T_e)$	4.2	44
e ^H + Ar ^m → Ar ⁺ + e	$k_{miz}^H = 5.7 \times 10^{-13} T_e^{-0.33} \exp(-6.82/T_e)$	4.2	48
e + Cu → Cu ⁺ + 2e	$k_{Miz} = k_{Miz}^H = 3.898 \times 10^{-14} \times T_e^{0.484} \exp(-7.1344/T_e)$	7.68	9
e + Cu → Cu + e	$k_{Mel} = 1.03 \times 10^{-11} T_e^{-0.607} \exp(-8.98/T_e)$	-	49
Ar ^m + Cu → Ar + Cu ⁺ + e	$k_p = 2.36 \times 10^{-16}$	-4.46	50
Ar ⁺ + Cu → Ar + Cu ⁺	$k_{chexc} = 2 \times 10^{-16}$	-	51

For Ar^H, the rate equation is

$$\frac{dn_{Ar^H}}{dt} = -(k_{iz}n_e + k_{iz}^H n_{e^H})n_{Ar^H} - (k_{ex}n_e + k_{ex}^H n_{e^H})n_{Ar^H} - \Gamma_{Ar^H,diff} \frac{S_{IR} - S_T}{V_{IR}} + \Gamma_{Ar^+} \frac{S_T}{V_{IR}} + \Gamma_{Ar^H,HCE} \frac{S_{IR} - S_T}{V_{IR}}. \quad (A4)$$

The rate equation for Cu atoms is

$$\frac{dn_{Cu}}{dt} = -(k_{Miz}n_e + k_{Miz}^H n_{e^H})n_{Cu} - k_p n_{Ar^m} n_{Cu} - k_{chexc} n_{Ar^+} n_{Cu} - \Gamma_{Cu,diff} \frac{S_{IR} - S_T}{V_{IR}} + \Gamma_{Cu,HCE} \frac{S_{IR} - S_T}{V_{IR}} + (\Gamma_{Ar^+} Y_{Ar^+} + \Gamma_{Cu^+} Y_{Cu^+}) \frac{S_T}{V_{IR}}. \quad (A5)$$

The term $\Gamma_{Cu,diff}$ presents the diffusion flux of Cu without collision. It can be expressed by $\Gamma_{Cu,diff} = \Gamma_{Cu,0}(1 - F_{coll})$. $\Gamma_{Cu^+} = 0.4n_{Cu^+} u_{bohm,Cu^+}$ is the flux of Cu⁺ leaving the ionization region. Y_{Ar^+} and Y_{Cu^+} are the sputtering yields of Ar⁺ and Cu⁺ with Cu target and can be calculated by the TRIM software, as shown in the following equation $Y = aU^b$. U is the discharge voltage. For Cu⁺, the fitting parameters are $a = 0.0691$ and $b = 0.556$. For Ar⁺, the fitting parameters are $a = 0.1421$ and $b = 0.468$.

Similar to Ar⁺, the rate equation for Cu⁺ can be described as

$$\frac{dn_{Cu^+}}{dt} = (k_{Miz}n_e + k_{Miz}^H n_{e^H})n_{Cu} + k_p n_{Ar^m} n_{Cu} + k_{chexc} n_{Ar^+} n_{Cu} + \Gamma_{Cu^+,HCE} \frac{(S_{IR} - S_T)}{V_{IR}} - \Gamma_{Cu^+} \frac{S_T + (S_{IR} - S_T)(1 - \beta_{Cu^+})}{V_{IR}}. \quad (A6)$$

2. Particle balance for electrons

The rate equation for the electrons is

$$\frac{dn_e}{dt} = (k_{iz}n_e + k_{iz}^H n_{e^H})(n_{Ar} + n_{Ar^H}) + (k_{miz}n_e + k_{miz}^H n_{e^H})n_{Ar^m} + (k_{Miz}n_e + k_{Miz}^H n_{e^H})n_{Cu} + k_p n_{Cu} n_{Ar^m} - \Gamma_e \frac{S_{IR} - S_T}{V_{IR}} + \Gamma_{e,HCE} \frac{S_{IR} - S_T}{V_{IR}}, \quad (A7)$$

where the electron flux can be expressed as $\Gamma_e \approx 0.4n_e \frac{D_e}{R_{IR}} \left(1 + \frac{U_{IR}}{T_e}\right)$. $D_e = \frac{1}{\omega r} \frac{T_e}{B}$ is the Bohm diffusion coefficient of electrons. $B = 45$ mT is the simulated average magnetic field at the ionization region boundary. The potential drop in the ionization region U_{IR} can be calculated by the simplified Poisson equation

$$U_{IR} = -\frac{eR_{IR}^2}{\epsilon_0} (n_{Ar^+} + n_{Cu^+} - n_e - n_{e^H}). \quad (A8)$$

The rate equation of the hot electrons is expressed as

$$\frac{dn_{e^H}}{dt} = \frac{1}{eU_D/2} \left(\frac{U_{SH} I_{se}}{V_{IR}} - Q^H \right), \quad (A9)$$

in which U_D is the pulse voltage and $U_{SH} = U_D - U_{IR}$ is the

sheath voltage. $I_{se} = eS_T(\gamma_{Ar^+}\Gamma_{Ar^+} + \gamma_{Cu^+}\Gamma_{Cu^+})$ is the secondary electron current, where γ is the secondary electron emission coefficient. In this model, $\gamma_{Ar^+} = 0.112$ and $\gamma_{Cu^+} = 0$. Q^H is the energy loss of hot electrons in the inelastic collision with the atoms³⁸

$$\frac{Q^H}{e} = (E_{Ar,c} + E_{htc})k_{iz}^H n_{e^H}(n_{Ar} + n_{Ar^H}) + (E_{Ar^m,c} + E_{htc})k_{miz}^H n_{e^H} n_{Ar^m} + (E_{Cu,c} + E_{htc})k_{Miz}^H n_{e^H} n_{Cu} - E_{dex} k_{dex}^H n_{e^H} n_{Ar^m}. \quad (A10)$$

3. Energy balance

T_e is obtained by solving the energy balance equation, as Eq. (A11)

$$\begin{aligned} \frac{d}{dt} \left(\frac{3}{2} e n_e T_e \right) &= F_{PWR} \frac{P_D}{V_{IR}} - Q \\ &- \left[\frac{3}{2} e T_e \Gamma_e \frac{S_{IR} - S_T}{V_{IR}} + \sum_{i=Ar^+, Cu^+} \frac{1}{2} e T_e \Gamma_i \frac{S_T + (S_{IR} - S_T)(1 - \beta_i)}{V_{IR}} \right]. \end{aligned} \quad (A11)$$

$P_D = U_D \times I_D$ is the instantaneous power of the discharge pulse though which the experimental pulse shapes are implemented in the global model. Q includes the energy losses by electron impact ionization with neutral atoms (Ar, Ar^m, Ar^H, and Cu) and the energy released by the deexcitation and the Penning ionization, as shown below:

$$\begin{aligned} \frac{Q}{e} &= E_{Ar,c} k_{iz} n_e (n_{Ar} + n_{Ar^H}) + E_{Ar^m,c} k_{miz} n_e n_{Ar^m} \\ &+ E_{Cu,c} k_{Miz} n_e n_{Cu} - E_{dex} k_{dex} n_e n_{Ar^m} - E_p k_p n_{Cu} n_{Ar^m}, \end{aligned} \quad (A12)$$

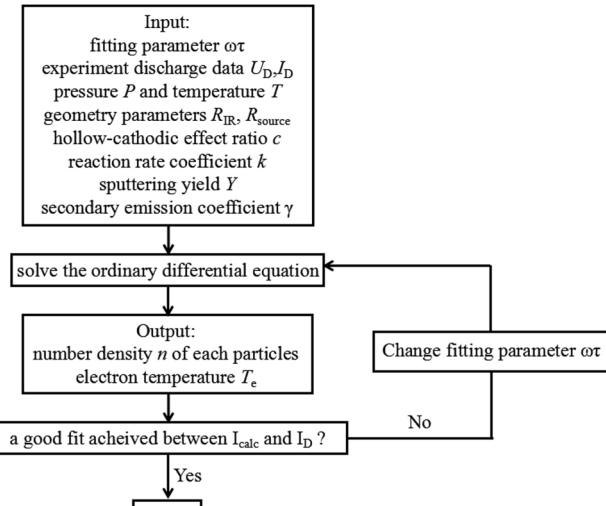


FIG. 12. Flow chart of the global model.

TABLE IV. Parameter table of the global model.

Symbol	Meaning	Unit
$\omega\tau$	Hall parameter (fitting parameter)	
B	Average magnetic field at the ionization region boundary	45 mT
I_D	Experiment discharge current	A
U_D	Experiment discharge voltage	V
P	Pressure	1 Pa
T	Gas temperature	300 K
R_{IR}	The radius of the ionization region	1.5 cm
R_{source}	The radius of the cylindrical cathode	6 cm
S_T	The contact area of the ionization region with the target	113.1 cm ²
S_{IR}	Ionization region superficial area	262.5 cm ²
V_{IR}	Ionization region volume	119.1 cm ³
k	Reaction coefficient	m ³ /s
γ	The secondary electron emission coefficient	
Y	Sputtering yield	
c	Hollow cathode effect ratio	
T_e	Electron temperature	eV
n	Number density	1/m ³
I_{calc}	Simulated discharge current	A
α	Ionization rate	
β	Ion return probability	

The collisional energy losses per electron-ion pair are described as

$$\begin{aligned} k_{iz}E_{Ar,c} &= k_{iz}E_{iz} + k_{ex}E_{ex} + k_{el}\frac{3m_e}{m_{Ar}}T_e, \\ k_{miz}E_{Ar^m,c} &= k_{miz}E_{iz} + k_{el}\frac{3m_e}{m_{Ar}}T_e, \\ k_{Miz}E_{Cu,c} &= k_{Miz}E_{Miz} + k_{Me}\frac{3m_e}{m_{Cu}}T_e. \end{aligned} \quad (\text{A13})$$

The ion return probability β can be expressed:

$$\beta_i = \begin{cases} 0 & U_{IR} \leq T_i \\ 1 - \frac{T_i}{U_{IR}} & U_{IR} > T_i \end{cases} \quad i = Ar^+, Cu^+. \quad (\text{A14})$$

Figure 12 is the flow chart of the global model and reveals the determined method of the free parameter $\omega\tau$

$$I_{calc} = e\Gamma_{Ar^+}S_T(1 + \gamma_{Ar^+}) + e\Gamma_{Cu^+}S_T(1 + \gamma_{Cu^+}), \quad (\text{A15})$$

where I_{calc} is the simulated discharge current which is used to fit the experiment current I_D .

The input and output parameters of the global model are shown in Table IV.

REFERENCES

- V. Kouznetsov, K. Macák, J. M. Schneider, U. Helmersson, and I. Petrov, *Surf. Coat. Technol.* **122**, 290 (1999).
- J. Alami, J. T. Gudmundsson, J. Bohlmark, J. Birch, and U. Helmersson, *Plasma Sources Sci. Technol.* **14**, 525 (2005).
- J. T. Gudmundsson, P. Sigurjonsson, P. Larsson, D. Lundin, and U. Helmersson, *J. Appl. Phys.* **105**, 123302 (2009).
- J. Bohlmark, J. Alami, C. Christou, A. P. Ehiasarian, and U. Helmersson, *J. Vac. Sci. Technol. A* **23**, 18 (2005).
- E. Oks and A. Anders, *J. Appl. Phys.* **105**, 093304 (2009).
- Z. Z. Wu, X. B. Tian, F. Pan, R. K. Y. Fu, and P. K. Chu, *Acta Phys. Sin.* **63**, 185207 (2014).
- A. Anders, *Surf. Coat. Technol.* **205**, S1 (2011).
- A. P. Ehiasarian, J. G. Wen, and I. J. Petrov, *Appl. Phys.* **101**, 054301 (2007).
- M. Samuelsson, D. Lundin, J. Jensen, M. Raadu, J. T. Gudmundsson, and U. Helmersson, *Surf. Coat. Technol.* **205**, 591 (2010).
- J. S. Colligon, *J. Vac. Sci. Technol. A* **13**, 1649 (1995).
- J. W. Lim, H. S. Park, T. H. Park, J. J. Lee, and J. Joo, *J. Vac. Sci. Technol. A* **18**, 524 (2000).
- J. Alami, P. O. A. Persson, D. Music, J. T. Gudmundsson, J. Bohmark, and U. Helmersson, *J. Vac. Sci. Technol. A* **23**, 278 (2005).
- K. Sarakinos, J. Alami, and S. Konstantinidis, *Surf. Coat. Technol.* **204**, 1661 (2010).
- Z. Z. Wu, X. B. Tian, F. Pan, R. K. Y. Fu, and P. K. Chu, *Acta Meta. Sin.* **10**, 1279 (2014).
- J. Lin, J. J. Moore, W. D. Sproul, B. Mishra, J. A. Rees, and Z. Wu, *Surf. Coat. Technol.* **203**, 3676 (2009).
- X. Qin, P. Ke, A. Wang, and K. H. Kim, *Surf. Coat. Technol.* **228**, 275 (2013).
- N. Holtzer, O. Antonin, T. Minea, S. Marnieros, and D. Bouchier, *Surf. Coat. Technol.* **250**, 32 (2014).
- J. Olejníček, Z. Hubička, and Š Kment, *Surf. Coat. Technol.* **232**, 376 (2013).
- U. Helmersson, in 2011 Proceedings of 11th International Workshop on Plasma Based Ion Implantation & Deposition Harbin (Surface & Coatings Technology, Harbin, 2011), p. 21.
- D. A. Karpov, *Surf. Coat. Technol.* **96**, 22 (1997).
- S. Xiao, Z. Z. Wu, S. H. Cui, L. L. Liu, B. C. Zheng, H. Lin, R. K. Y. Fu, X. B. Tian, F. Pan, and P. K. Chu, *Acta Phys. Sin.* **65**, 185202 (2016).
- S. H. Cui, Z. Z. Wu, S. Xiao, L. L. Liu, B. C. Zheng, H. Lin, R. K. Y. Fu, X. B. Tian, P. K. Chu, W. C. Tan, and F. Pan, *Acta Phys. Sin.* **66**, 095203 (2017).
- M. A. Lieberman, *J. Appl. Phys.* **66**, 2926 (1989).
- J. T. Scheuer, M. Shamim, and J. R. Conrad, *J. Appl. Phys.* **67**, 1241 (1990).
- G. A. Emmert and M. A. Henry, *J. Appl. Phys.* **71**, 113 (1992).
- M. Widner, I. Alexeff, W. D. Jones, and K. E. Lonngren, *Phys. Fluids* **13**, 2532 (1970).
- Z. Y. Xia and C. Chan, *J. Appl. Phys.* **73**, 3651 (1993).
- J. M. Dawson, *Rev. Mod. Phys.* **55**, 403 (1983).
- V. Vahedi and M. Surendra, *Comput. Phys. Commun.* **87**, 179 (1995).
- S. Kim, M. A. Lieberman, A. J. Lichtenberg, and J. T. Gudmundsson, *J. Vac. Sci. Technol. A* **24**, 2025 (2006).
- J. T. Gudmundsson and E. G. Thorsteinsson, *Plasma Sources Sci. Technol.* **16**, 399 (2007).
- E. G. Thorsteinsson and J. T. Gudmundsson, *Plasma Sources Sci. Technol.* **18**, 045002 (2009).
- M. A. Lieberman and R. A. Gottscho, *Phys. Thin Films* **18**, 1 (1994).
- C. Lee, D. B. Graves, M. A. Lieberman, and D. W. Hess, *J. Electrochem. Soc.* **141**, 1546 (1994).
- C. Lee and M. A. Lieberman, *J. Vac. Sci. Technol. A* **13**, 368 (1995).
- J. T. Gudmundsson, in 2008 Proceedings of the 17th International Vacuum Congress/13th International Conference on Surface Science/international Conference on Nanoscience and Technology (Journal of Physics Conference Series, 2008), p. 082013.
- S. Ashida, C. Lee, and M. A. Lieberman, *J. Vac. Sci. Technol. A* **13**, 2498 (1995).
- B. C. Zheng, D. Meng, H. L. Che, and M. K. Lei, *J. Appl. Phys.* **117**, 203302 (2015).
- M. Liang, Y. He, M. M. Szott, J. T. McLain, and D. N. Ruzic, *J. Appl. Phys.* **115**, 223301 (2014).
- A. Anders and J. Andersson, *J. Appl. Phys.* **102**, 113303 (2007).
- A. Mishra, P. J. Kelly, and J. W. Bradley, *Plasma Sources Sci. Technol.* **19**, 045014 (2010).
- B. Liebig and J. W. Bradley, *Plasma Sources Sci. Technol.* **22**, 045020 (2013).
- B. C. Zheng, Z. L. Wu, B. Wu, Y. G. Li, and M. K. Lei, *J. Appl. Phys.* **121**, 171901 (2017).
- M. Raadu, I. Axnäs, J. Gudmundsson, C. Huo, and N. Brenning, *Plasma Sources Sci. Technol.* **20**, 065007 (2011).

- ⁴⁵M. A. Lieberman and A. J. Lichtenberg, *Principles of Plasma Discharges and Materials Processing* (John Wiley & Sons Inc., 2005).
- ⁴⁶N. J. Mason and W. R. Newell, *J. Phys. B* **20**, 1357 (1987).
- ⁴⁷V. Puech and L. Torchin, *J. Phys. D* **19**, 2309 (1986).
- ⁴⁸H. A. Hyman, *Phys. Rev. A* **20**, 855 (1979).
- ⁴⁹S. Trajmar, W. Williams, and S. K. Srivastava, *J. Phys. B* **10**, 3323 (1977).
- ⁵⁰A. Bogaerts, R. Gijbels, and R. J. Carman, *Spectrochim. Acta B* **53**, 1679 (1998).
- ⁵¹S. C. Rae and R. C. Tobin, *J. Appl. Phys.* **64**, 1418 (1988).